THE JOURNAL OF PHYSICAL CHEMISTRY B

Article

pubs.acs.org/JPCB

Computational Study of the $Fe(CN)_2CO$ Cofactor and Its Binding to HypC Protein

Marta Albareda,[†,‡] Jose-Manuel Palacios,[†,‡] Juan Imperial,[†,‡,§] and Luis F. Pacios*[,†,∥]

[†]Centro de Biotecnología y Genómica de Plantas (CBGP), Universidad Politécnica de Madrid (UPM), Campus de Montegancedo, 28223 Madrid, Spain

[‡]Departamento de Biotecnología, ETSI Agrónomos, UPM, 28040 Madrid, Spain

[§]Consejo Superior de Investigaciones Científicas, CBGP, UPM, 28223 Madrid, Spain

[∥]Departamento de Biotecnología, ETSI Montes, UPM, 28040 Madrid, Spain

Supporting Information

ABSTRACT: In the intricate maturation process of [NiFe]-hydrogenases, the $Fe(CN)_2CO$ cofactor is first assembled in a HypCD complex with iron coordinated by cysteines from both proteins and CO is added after ligation of cyanides. The small accessory protein HypC is known to play a role in delivering the cofactor needed for assembling the hydrogenase active site. However, the chemical nature of the $Fe(CN)_2CO$ moiety and the stability of the cofactor−HypC complex are open questions. In this work, we address geometries, properties, and the nature of bonding of all chemical species involved in formation and binding of the cofactor by means of quantum calculations. We also study the influence of environmental effects and binding to cysteines on vibrational frequencies of stretching modes of CO and CN used to detect the presence of $Fe(CN)_2CO$. Carbon monoxide is found to be much more sensitive to sulfur binding and the polarity of the medium than cyanides. The stability of the HypC−cofactor complex is analyzed by means of molecular dynamics simulation of cofactor-free and cofactor-bound forms of HypC. The results show that HypC is stable enough to carry the cofactor, but since its binding cysteine is located at the N-terminal unstructured tail, it presents large motions in solution, which suggests the need for a guiding interaction to achieve delivery of the cofactor.

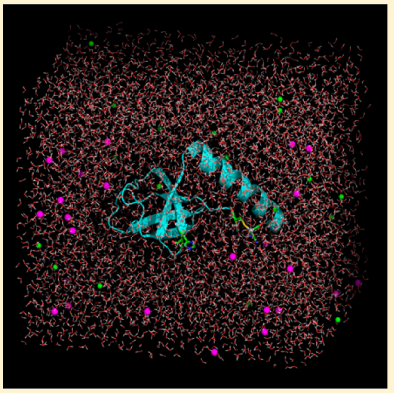

INTRODUCTION

[NiFe]-hydrogenases are heterodimeric enzymes that catalyze the reversible oxidation of molecular hydrogen $H_2 \leftrightarrow 2H^+ + 2e^-$ in a broad range of microorganisms. These enzymes usually comprise a small subunit of about 30 kDa with iron−sulfur clusters responsible for electron transfer to and from the active site in a large subunit of about 65 kDa responsible for catalysis.[1,2] The large subunit contains within the active center a NiFe−$(CN)_2CO$ cofactor unique in nature[3] whose electron density has been detected by X-ray crystallography in several bacteria.[4−6] The synthesis and insertion of this cofactor into the hydrogenase large subunit is a complex process that involves six specific maturation proteins named HypA, B, C, D, E, and F.[7] Two of these proteins, HypA and HypB (and SlyD in the case of *Escherichia coli*), catalyze the acquisition and insertion of nickel once the $Fe(CN)_2CO$ cofactor is installed in the large subunit.[8] The CN^- ligands are synthesized from carbamoyl-phosphate through the concerted action of HypE and HypF proteins.[9]

According to the current view of [NiFe]-hydrogenase active site assembly,[10] the iron−sulfur protein HypD that contains a [4Fe−4S] cluster and the accessory protein HypC form a complex in which both structures are connected through an iron ion that is ligated by one conserved cysteine residue of each protein.[11−14] HypC is a small, 9.6 kDa protein consisting of a β-barrel binding domain joined to a C-terminal α-helix through a flexible loop. The N-terminal coil adopts an extended conformation, which allows the conserved essential C2 residue to make contact with the solvent and interact with partner proteins in complexes (see below). Watanabe and co-workers have structurally characterized these proteins from *Thermococcus kodakaraensis* reporting X-ray structures of isolated HypC and HypD at 1.8 and 2.07 Å resolution, respectively,[11] and the HypCD complex at 2.55 Å resolution,[14] although several residues (including HypC−C2) are missing in this latter case.

Infrared spectroscopy has demonstrated that purified HypCD complexes from *Ralstonia eutropha* and *E. coli* exhibit absorption bands characteristic of diatomic CN^- and CO ligands,[12,15] which suggests that the HypCD complex is the assembly site of the $Fe(CN)_2CO$ cofactor. However, Stripp et al. have shown very recently that HypD isolated in the absence of HypC exhibits infrared bands indistinguishable from those observed for the HypCD complex at 1956, 2072, and 2092 cm^{-1} which can be assigned to $\nu(CO)$, $\nu(CN^-)_{asym}$, and

Received: July 30, 2013
Revised: September 9, 2013
Published: October 4, 2013

dx.doi.org/10.1021/jp407574n | *J. Phys. Chem. B* 2013, 117, 13523−13533

$\nu(CN^-)_{sym}$, respectively,[13] demonstrating thus that HypD carries the complete $Fe(CN)_2CO$ cofactor. Nevertheless, HypC is known to play key roles at this stage of the maturation process: on one side, purification of HypCD needs coexpression of *hypC* and *hypD* genes.[16] On the other side, available evidence indicates that HypC might participate in the delivery of the $Fe(CN)_2CO$ cofactor to its destination substrate[17] even though it has been suggested that the cofactor-bound form of HypC might be unstable,[13] an issue which is here addressed by means of molecular dynamics (MD) simulations.

Besides the three unusual diatomic ligands in the form of two cyanides and one carbon monoxide, iron is ligated by one or two sulfur atoms depending on whether the $Fe(CN)_2CO$ cofactor is bound to one cysteine of either protein or two cysteines in the HypCD complex, yielding thus a 4-fold or 5-fold coordination structure. Although a molecular modeling study[18] has been reported for a representative geometry of the complete NiFe−$(CN)_2CO$ cofactor inside the large subunit of [NiFe]-hydrogenases,[3−6,10] the chemical nature of the $Fe(CN)_2CO$ moiety has received little attention from a theoretical point of view. Furthermore, the dynamical stability of the HypC protein in the absence and in the presence of the $Fe(CN)_2CO$ cofactor has not been addressed yet.

In this work, we aimed to fill this gap as follows. (1) DFT quantum calculations were performed to obtain optimized geometries and vibrational frequencies of all the species related to formation and binding of the cofactor. (2) The nature of bonding especially in Fe−CN^- and Fe−CO links was explored by means of the topological analysis of the electron density. (3) The influence of the environment on the vibrational frequencies of CO and CN^- ligands was studied by carrying out SCRF-PCM (self-consistent reaction field−polarizable continuum model)[19] calculations in five media of increasing polarity from vacuum (ε = 1) to water (ε = 78.36). (4) A model of the cofactor site in the crystal structure of the HypCD complex from *T. kodakaraensis* constructed upon completing missing residues in X-ray data (particularly, the iron-binding HypC−C2) together with the $Fe(CN)_2CO$ cofactor itself is presented. (5) Adding to our previous research on the synthesis of the active hydrogenase in the endosymbiotic bacterium *Rhizobium leguminosarum*,[20−22] a model for the structure of its HypC protein was generated. The stability of isolated and cofactor-bound forms of HypC from *R. leguminosarum* was finally investigated by means of MD simulations.

While (1) and (2) aim at gaining insight into the chemical nature of the cofactor, (3) tries to assess the distinct dependence of reference CO and CN^- vibrational frequencies on the polarity of the medium in order to identify the more sensitive ligand to the protein environment in the binding site. (1)−(3) are addressed by performing DFT quantum calculations. The purpose of (4) is to provide a complete model of the cofactor inserted into the HypCD complex in order to identify other residues that might also be involved in the interaction. Finally, since HypC is part of a large multiprotein complex and possibly mediates protein recognition, with the MD study (5) we aim to explore its structural stability in the absence and in the presence of the cofactor at an initial geometry provided by the previous quantum calculations.

COMPUTATIONAL METHODS

Quantum Calculations. In what follows, $Fe^{2+}(CN^-)_2$ is just abbreviated as $Fe(CN)_2$ and binding cysteines are represented by CH_3CH_2SH molecules herein denoted Et−SH. The following species involved in formation and binding of the cofactor with and without the CO ligand were considered: $Fe(CN)_2CO$, Et−S−$Fe(CN)_2CO$, $(Et-S)_2$−$Fe(CN)_2CO$, $Fe(CN)_2$, Et−S−$Fe(CN)_2$, and $(Et-S)_2$−$Fe(CN)_2$ (Figure 1; atom numbering in Figure S1 in the Supporting Information). Geometries were optimized using analytic gradients without symmetry constraints at DFT calculations with the hybrid B3LYP functional and Ahlrichs's TZVP basis sets.[23] To estimate the influence of environment on the vibrational frequencies of cyanide and carbon monoxide ligands, harmonic frequencies were obtained in SCRF-PCM[19] B3LYP/TZVP calculations in five media of increasing polarity given by ε = 1, 2, 4, 40, and 78.36 (water). Dielectric constants 2 and 4 are customarily used for protein interiors, whereas the higher ε = 40 has been used for solvent-exposed regions in proteins.[24] Two further sets of single point calculations were performed at the optimized geometries to (1) obtain the electron density $\rho(\mathbf{r})$ for the topological analysis and (2) compute atomic charges fit to the electrostatic potential at points selected according to the CHelpG scheme.[25] Bond critical points (BCPs) of $\rho(\mathbf{r})$ were localized and characterized according to the atoms in molecules (AIM) theory[26,27] with Extreme.[28] All quantum calculations were performed with Gaussian 09.[29]

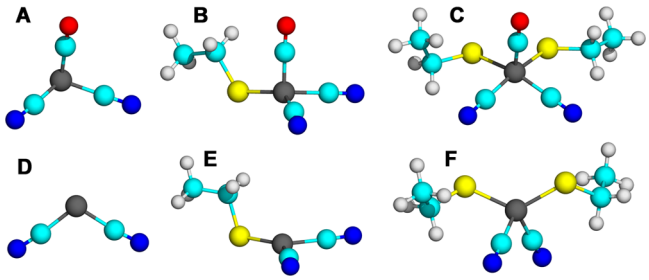

Figure 1. B3LYP/TZVP geometries of (A) $Fe(CN)_2CO$, (B) Et−S−$Fe(CN)_2CO$, (C) $(Et-S)_2$−$Fe(CN)_2CO$, (D) $Fe(CN)_2$, (E) Et−S−$Fe(CN)_2$, (F) $(Et-S)_2$−$Fe(CN)_2$. (Fe, gray; C, cyan; N, blue; O, red; S, yellow; H, white).

Force Field Parameters of $Fe(CN)_2CO$ Cofactor. CHARMM[30] force field parameters for MD calculations were obtained for the cofactor as follows. The geometry of $Fe(CN)_2CO$ was reoptimized in internal coordinates in B3LYP/TZVP calculations to obtain equilibrium bond lengths, angles, and dihedrals. Templates for the residue topology file (RTF) that includes the internal coordinate table and the parameter file (PAR) with the necessary geometry data as well as force constants and Lennard-Jones potential parameters were obtained from the SwissParam server[31] upon using a model organic compound of formula $N(CN)_2CO$. A further "IntModes" frequencies calculation was performed for $Fe(CN)_2CO$ to obtain the Hessian tensor, and the program FUERZA was employed to determine internal force constants from Cartesian second derivatives. This program implements a first-principles method which avoids fitting procedures and is fully invariant to the choice of internal coordinates.[32,33] Data in template files were then substituted for the corresponding values of $Fe(CN)_2CO$ upon using standard CHARMM 3.1 non-bonded parameters for Fe(II) ion and CHelpG atomic charges for the cofactor. The resulting RTF and PAR files are given in Tables S1 and S2 in the Supporting Information, respectively. It must be mentioned that parameters developed

dx.doi.org/10.1021/jp407574n | J. Phys. Chem. B 2013, 117, 13523−13533

for a different force field for the complete NiFe metal cluster bonded to four cysteines and one OH group bridging Fe and Ni atoms in the [NiFe]-hydrogenase large subunit of *R. eutropha* have been reported upon following a frequency-matching methodology to obtain force constants.[34]

Protein Modeling. The structural model of HypC protein from *R. leguminosarum* was generated by homology modeling with SwissModel[35,36] using as a template the chain B of HypC crystal structure from *T. kodakaraensis*.[11] Although the sequence identity between both HypC proteins is not high (34.25%), the resulting model structure for the *R. leguminosarum* protein shows a satisfactory quality estimate (QMEAN[37] *Z*-score = −0.342) and is virtually identical to the crystal structure of the template ($RMS_{\alpha Carbons}$ = 0.395 Å; Figure S2 in the Supporting Information). Given that the first residue in this model structure is C2 and that molecular mechanics (MM) and MD calculations add hydrogens, we first added the N-terminal M1 amino acid optimizing the resulting structure with SwissPdbViewer[38] to avoid having the charged NH_3^+ group at C2. The $Fe(CN)_2CO$ cofactor was then added to HypC−C2 with Chimera.[39] Since the resulting HypC−cofactor complex was to be subsequently subjected to MD calculations in water (see below), this preliminary geometry was preoptimized *in vacuo* with the AutoIMD module of VMD 1.9.1[40] doing a CHARMM 3.1[30] minimization with NAMD 2.9.[41]

In the crystal structure of the HypCD complex from *T. kodakaraensis* (PDB code 3VYR), the key C2 amino acid of HypC as well as the $Fe(CN)_2CO$ cofactor itself are absent.[14] To obtain a complete model of this complex, we used a docking complex between HypC and HypD from *T. kodakaraensis* (PDB codes 2Z1C and 2Z1D, respectively)[11] that we had prepared with ClusPro 2.0[42] before this crystal structure was published. This docking complex was similar to the released experimental structure of HypCD, particularly at the region in which the N-terminal coil of HypC contacts the binding site of HypD. The great resemblance between HypC structures from both *T. kodakaraensis* and *R. leguminosarum* allowed us to superimpose the full HypC protein from *R. leguminosarum* with the bound cofactor to obtain a complete model of the HypCD complex including both the HypC−C2 amino acid and the cofactor. This model was subsequently optimized in the presence of water with NAMD[41] calculations (see next subsection) to obtain the final geometry at the cofactor site discussed below.

Molecular Dynamics (MD) Simulations. MD simulations with the CHARMM 3.1[30] force field were performed with NAMD 2.9[41] for both isolated and cofactor-bound forms of the HypC protein from *R. leguminosarum*. Initial structures were immersed in periodic rectangular solvation boxes containing 6820 water molecules added according to the TIP3P model[43] together with Na^+ and Cl^- ions added to counter the total negative charge of the systems while providing 0.150 M salt concentration. The particle mesh Ewald summation method[44] was used for long-range electrostatics, and a 10 Å cutoff was set for short-range non-bonded interactions. A first optimization of every system was carried out along 5000 conjugate gradient minimization steps. With all atoms fixed in proteins, water was then equilibrated for 100 ps at 2 fs time steps at 298 K and 1 atm. Keeping the same time steps, T and P, simulation runs were then performed in the NPT ensemble during 10 ns (5 million steps). Langevin dynamics for the T control and the Nosé−Hoover Langevin piston method for the P control were employed. Output trajectories were processed and analyzed with VMD 1.9.1,[40] Carma,[45] and MDTRA[46] programs.

Molecular Graphics. All the molecular graphics were prepared and rendered with PyMOL 1.5.[47]

RESULTS AND DISCUSSION

Quantum Geometries. According to the current model on the maturation pathway for [NiFe]-hydrogenases, HypD is the scaffold on which iron receives the CN^- ligands from HypE.[9,11,16] Although many details still remain unclear, a cyanation reaction mechanism for the incorporation of two CN^- ligands to HypD has been proposed. As for this proposed mechanism, the final steps of modification of the iron atom involve the transfer of carbon monoxide ligand.[11] In addition, Bürstel et al. have provided experimental evidence that the attachment of CN^- ligands is a prerequisite for subsequent CO binding.[15] We therefore assumed the preexistence of a $Fe(CN)_2$ moiety prior to the incorporation of carbon monoxide in obtaining the geometries of chemical species involved in the binding of the cofactor.

Optimized geometries of $Fe(CN)_2CO$, Et−S−$Fe(CN)_2CO$, $(Et-S)_2$−$Fe(CN)_2CO$, and the corresponding species without CO are shown in Figure 1. The $Fe(CN)_2CO$ segments of complete NiFe cofactors which are bound to four cysteines and have OH groups bridging Fe and Ni atoms[18] in crystal structures of large subunits of hydrogenases from *Allochromatium vinosum* (PDB code 3MYR),[4] *R. eutropha* (3RGW),[5] and *Hydrogenovibrio marinus* (3AYX)[48] were taken as reference examples to superimpose the computed geometry of Fe-$(CN)_2CO$ (Figure 2). Representative bond distances for

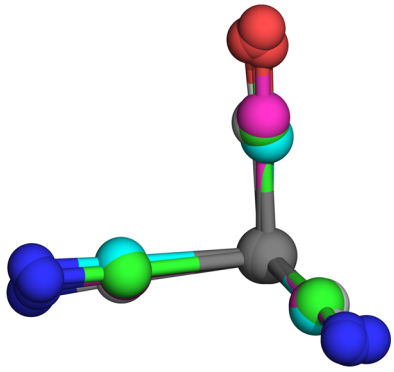

Figure 2. Superposition of the quantum geometry of $Fe(CN)_2CO$ cofactor (C in white) and the corresponding part of the complete NiFe cofactor in crystal structures of large subunits of hydrogenases from *R. eutropha* (PDB code 3RGW, C in pink), *H. marinus* (PDB code 3AYX, C in green), and *A. vinosum* (PDB code 3MYR, C in cyan) (Fe, gray; N, blue; O, red).

quantum geometries obtained in the gas phase and in water as well as the values for the corresponding species without CO are collected in Table 1 (B3LYP/TZVP calculated bond lengths for CN^- anion and CO diatomics are 1.172 and 1.127 Å, respectively). Relevant bond angles for quantum geometries are given in Table 2.

Quantum calculations for isolated $Fe(CN)_2CO$ cofactor provide a fairly good representation when compared with corresponding segments in NiFe complete final cofactors (Figure 2). The somewhat anomalous values shown by both Fe−(CO) and CO bond lengths in the X-ray structures (Table 1) suggest that carbon monoxide at the binding site in some

dx.doi.org/10.1021/jp407574n | J. Phys. Chem. B 2013, 117, 13523−13533

Table 1. Bond Lengths in Species Involved in the Binding of $Fe(CN)_2CO$ Cofactor[a]

	Fe−$(CN)_1$	Fe−$(CN)_2$	Fe−(CO)	$(CN)_1$	$(CN)_2$	CO	Fe−S_1	Fe−S_2
				$(Et-S)_2-Fe(CN)_2CO$[b]				
CO present	1.946	1.949	1.713	1.170	1.167	1.161	2.355	2.345
ibid in water	1.935	1.936	1.717	1.167	1.167	1.157	2.332	2.322
no CO	1.906	1.908		1.170	1.170		2.291	2.283
				$Et-S-Fe(CN)_2CO$[b]				
CO present	1.905	1.906	1.728	1.163	1.163	1.150	2.203	
ibid in water	1.921	1.920	1.739	1.164	1.164	1.147	2.210	
no CO	1.909	1.910		1.160	1.156		2.240	
				$Fe(CN)_2CO$[b]				
CO present	1.857	1.857	1.780	1.161	1.161	1.132		
ibid in water	1.893	1.894	1.792	1.161	1.161	1.134		
no CO	1.863	1.863		1.161	1.161			
				$(Et-S)_2-Fe(CN)_2CO$ Part of the NiFe Final Cofactor				
X-ray[c]	1.906	1.885	1.574	1.184	1.171	1.239	2.293	2.268
X-ray[d]	1.896	1.835	1.900	1.165	1.152	1.214	2.259	2.240
X-ray[e]	1.925	1.870	1.778	1.172	1.155	1.170	2.347	2.306

[a]Values in Å. Atom numbering refers to Figure S1 in the Supporting Information. [b]B3LYP/TZVP geometries, this work (Figure 1). [c]Data from crystal structures of hydrogenases from *A. vinosum*, PDB code 3MYR (ref 4). [d]Data from crystal structures of hydrogenases from *R. eutropha*, PDB code 3RGW (ref 5). [e]Data from crystal structures of hydrogenases from *H. marinus*, PDB code 3AYX (ref 48).

Table 2. Bond Angles in Species Involved in the Binding of $Fe(CN)_2CO$ Cofactor[a]

	$C_{CN1}FeC_{CN2}$	$C_{CO}FeC_{CN1}$	$C_{CO}FeC_{CN2}$	$C_{CN1}FeS_1$	$C_{CN2}FeS_1$	$C_{CO}FeS_1$	$C_{CN1}FeS_2$	$C_{CN2}FeS_2$	$C_{CO}FeS_2$	S_1FeS_2
					$(Et-S)_2-Fe(CN)_2CO$					
CO present	88.7	94.8	94.9	91.8	166.4	98.6	162.6	92.0	102.4	83.5
no CO	97.0			97.2	119.5		116.4	96.8		127.0
					$Et-S-Fe(CN)_2CO$					
CO present	92.7	95.3	95.3	130.7	131.1	100.7				
no CO	93.5			132.4	134.1					
					$Fe(CN)_2CO$					
CO present	106.1	93.6	93.5							
no CO	107.1									

[a]Values in degrees. B3LYP/TZVP geometries, this work (Figure 1). Atom numbering refers to Figure S1 in the Supporting Information.

Table 3. Atomic Charges of Selected Atoms and Groups around Iron in Species Involved in the Binding of $Fe(CN)_2CO$ Cofactor[a]

	Fe	$(CN)_1$	$(CN)_2$	(CO)	S_1	S_2
$Fe(CN)_2CO$	+0.7256	−0.3852	−0.3849	+0.0445		
$Et-S-Fe(CN)_2CO$	+0.4045	−0.4673	−0.4709	−0.0959	−0.5116	
$(Et-S)_2-Fe(CN)_2CO$	+0.3439	−0.5602	−0.5370	−0.1112	−0.5891	−0.6398
$Fe(CN)_2$	+0.8726	−0.4363	−0.4363			
$Et-S-Fe(CN)_2$	+0.5442	−0.5328	−0.5313		−0.6023	
$(Et-S)_2-Fe(CN)_2$	+0.6344	−0.6498	−0.6481		−0.7739	−0.7798

[a]Values in *e* calculated from the whole set of charges given in Table S3 of the Supporting Information. Atom numbering refers to Figure S1 in the Supporting Information.

mature hydrogenases might participate in interactions different from those of cyanide ligands. For instance, the binding site of *R. eutropha* hydrogenase reveals that the O atom of CO forms H-bonds with one N_η atom of R530 and with a backbone O atom of A528.[5] Quantum results in Table 1 reveal that Fe−CN distances increase and Fe−CO distances decrease with the incorporation of Et−S groups. However, while, in the presence of CO, the Fe−CN distance further increases about 0.04 Å with a second Et−S group, in the absence of CO, the Fe−CN distance remains unchanged. The intraligand distances also show a different behavior, with the CO bond length increasing noticeably with the incorporation of Et−S groups, whereas the CN bond length changes very little. These findings suggest that, when Fe is bound to S atoms, the bonding to cyanides weakens while the bonding to carbon monoxide strengthens, a result in agreement with the small decrease in CN and the large increase in CO found in the corresponding vibrational frequencies, particularly in polar environments (see below). Geometries optimized in the presence of water (not shown) produce structures rather similar to those obtained in the gas phase with differences scarcely significant.

Structures (Figure 1) and bond angles (Table 2) reveal that the cofactor changes from a distorded tetrahedron in $Fe(CN)_2CO$ to square pyramidal in both $Et-S-Fe(CN)_2CO$ and $(Et-S)_2-Fe(CN)_2CO$. In the latter structure, carbon monoxide makes a greater angle with sulfur than cyanide

dx.doi.org/10.1021/jp407574n | J. Phys. Chem. B 2013, 117, 13523−13533

Table 4. Topological Descriptors of Bond Critical Points (BCPs) of the Electron Density at Bond Paths in Species Involved in the Binding of $Fe(CN)_2CO$ Cofactor[a]

	Fe−C1	Fe−C2	Fe−C3	C1N1	C2N2	C3O3	Fe−S1, Fe−S2
				$Fe(CN)_2CO$			
ρ_c	0.1350	0.1350	0.1456	0.4792	0.4792	0.4858	
H_c	−0.0580	−0.0580	−0.0563	−0.9106	−0.9106	−0.8583	
ε	0.0851	0.0851	0.0950	0.0026	0.0026	0.0016	
				Et−S−$Fe(CN)_2CO$			
ρ_c	0.1184	0.1182	0.1647	0.4801	0.4801	0.4653	0.0932
H_c	−0.0435	−0.0434	−0.0733	−0.9149	−0.9150	−0.8134	−0.0342
ε	0.2467	0.2479	0.0459	0.0030	0.0030	0.0022	0.2406
				$(Et-S)_2$−$Fe(CN)_2CO$			
ρ_c	0.1048	0.1047	0.1697	0.4788	0.4788	0.4527	0.0661, 0.0678
H_c	−0.0330	−0.0328	−0.0777	−0.9129	−0.9130	−0.7854	−0.0182, −0.0190
ε	0.1589	0.1436	0.0414	0.0033	0.0033	0.0014	0.3123, 0.3222

[a]Descriptors computed at the BCP: ρ_c is the electron density, H_c is the total energy density, and ε is the ellipticity. ρ_c and H_c values in atomic units, ε is dimensionless. Atom numbering refers to Figure S1 in the Supporting Information.

ligands. In the absence of CO, the bonding of one Et−S group produces a planar structure around iron with a $C_{CN1}FeC_{CN2}$ angle considerably smaller than in the angular $Fe(CN)_2$ molecule, an expected result if one considers the presence of the S atom in the plane. The bonding of a second Et−S group gives rise to a tetrahedral-like arrangement around iron with a large SFeS angle (127°) and a small $C_{CN1}FeC_{CN2}$ angle (97°). However, the location of CN ligands is not symmetrical with respect to Et−S groups: $C_{CN1}FeS_1$ and $C_{CN2}FeS_2$ angles are 97°, whereas $C_{CN2}FeS_1$ and $C_{CN1}FeS_2$ angles are 116 and 119°, respectively. As for these results, the addition of carbon monoxide to the $Fe(CN)_2$ pre-cofactor bound to two cysteines, as it might occur in the HypCD complex, should involve a structural change with a torsion of the CN^- ligands around the iron atom and closing the SFeS angle to convert a tetrahedral structure (Figure 1F) into a pyramidal structure (Figure 1C).

Electron Properties and the Nature of Bonding. Atomic charges for atoms and groups around iron in all the species considered are presented in Table 3 (the whole set of atomic charges are collected in Table S3 in the Supporting Information). The isolated $Fe(CN)_2CO$ cofactor has a net zero charge, but the distinct bonding environments result in significant differences in atomic charges. Going from the isolated cofactor to one Et−S to two Et−S bonded groups, the negative charge of cyanides increases from −0.39*e* to −0.47*e* to −0.55*e*, the positive charge of iron decreases from +0.73*e* to +0.40*e* to +0.34*e*, and the small net charge of carbon monoxide changes very little. Moieties without CO show similar qualitative trends, yet in spite of its small net charge, the absence of CO produces greater values in all cases. As for the atomic charges, it is evident that the presence of CO produces a noticeable decrease in the charge polarization of the cofactor, particularly apparent in Fe: +0.73*e* in $Fe(CN)_2CO$ and +0.87*e* in $Fe(CN)_2$.

The information obtained from the topological analysis of $\rho(\mathbf{r})$ given by descriptors of its bond critical points (BCPs) sheds light on the nature of bonding. Typical covalent bonds are characterized by electron density values, ρ_c, greater than 0.3 au and large negative total energy densities, H_c, ∼−1.0 au,[26,27,49] whereas non-bonded interactions such as ionic attractions or H-bonds display a rather different magnitude. Conventional H-bonds have ρ_c in the range 0.002−0.04 au and very small positive values of H_c,[27,49] so that the presence of $\rho_c >$ 0.05 au and a negative small H_c is usually interpreted as a proof of strong interaction and the corresponding H-bond is assumed to have some degree of covalent character.[50−52] In the species related with $Fe(CN)_2CO$, topological descriptors (Table 4) distinguish two distinct types of bonding. Both ρ_c and H_c in CN and CO bonds are typical of pure covalent bonds, while Fe−C bond paths show features similar to those of strong H-bonds in proteins.[50−52] Even though these values belong to non-bonded (i.e., not purely covalent) interactions, they suggest a clear participation of covalent character.[26,27] For Fe−S bond paths, both ρ_c and H_c indicate also similar qualitative non-bonded interactions with covalent contribution.

Ellipticity, ε, adds additional information. This parameter measures the extent to which $\rho(\mathbf{r})$ is unequally distorted in perpendicular directions away from the bond axis, and its value correlates with the π-character of a bond.[26,27] For instance, the C—C bond in ethane and C≡C in ethyne have $\varepsilon \sim 0$ because $\rho(\mathbf{r})$ has symmetry along the bond axis, whereas ε of CC bonds in benzene increases to 0.176 and further to 0.298 for the double C═C bond in ethene. In molecules with conjugation effects, ε discriminates the different nature of bonding: C—C and C═C bonds in *trans*-1,3-butadiene show ε = 0.241 and 0.358, respectively.[27] Ellipticities in Table 4 also suggest different bonding types. Both CN and CO ligands have $\varepsilon \sim 0$ reminiscent of triple bond character, while 0.09 values in Fe−C bonds in isolated $Fe(CN)_2CO$ suggest non-negligible π-character. In Et−S−$Fe(CN)_2CO$, Fe−CN and Fe−S bonds reveal a greater π-character in supposedly single bonds, a feature reminiscent of conjugation effects. In $(Et-S)_2$−$Fe(CN)_2CO$, both Fe−CN bonds have a much smaller ε, while both Fe−S bonds show a large ε similar to double C═C bonds in organic compounds. Note that, whereas the presence of a single Et−S group produces similar sharing of π-character between both Fe−CN bonds and Fe−S bond, the link to two Et−S groups concentrates the π-character mainly in the Fe−S bond. Interestingly, the Fe−CO bond in sulfide-bound cofactors has ε even smaller than in the isolated cofactor, indicating that CO does not participate in the conjugation effect. This analysis points thus to a distinct behavior of CO: while in isolated $Fe(CN)_2CO$ the three ligands show a similar bonding, binding to sulfide produces a significant difference in the sense of introducing a π-character, conjugation-like effect in Fe−CN links.

Environmental Effects on Vibrational Frequencies of CN^- and CO Ligands. The IR spectroscopic identification of

dx.doi.org/10.1021/jp407574n | J. Phys. Chem. B 2013, 117, 13523−13533

the stretching modes of CN and CO has been widely used as a proof of the presence of $Fe(CN)_2CO$ either in HypCD complexes[12,15] or in complete final NiFe cofactors in mature [NiFe]-hydrogenases.[18,54] Very recently, the characteristic frequencies $\nu(CO)$ = 1956 cm^{-1}, $\nu(CN)_{asym}$ = 2072 cm^{-1}, and $\nu(CN)_{sym}$ = 2092 cm^{-1} have been identified by FT-IR spectroscopy also in HypD protein isolated in the absence of HypC.[13] On the theoretical side, a hybrid QM/MM approach to model the active site of the [NiFe]-hydrogenase from *R. eutropha* with the complete NiFe cofactor was used to compute IR spectra at DFT calculations.[18] Depending on details such as the number of atoms included in the QM part of the QM/MM model and the presence or absence of water, theoretical frequencies $\nu(CO)$ = [1950−1970] cm^{-1}, $\nu(CN)_{asym}$ = [2078−2106] cm^{-1}, and $\nu(CN)_{sym}$ = [2097−2128] cm^{-1} were obtained.[18]

With the aim to explore the distinct role of CO and CN ligands upon the different possible environments in a protein system depending on the exposure to solvent of a particular binding site, we performed SCRF-PCM calculations in five media of increasing polarity from vacuum (ε = 1) to water (ε = 78.36) to obtain B3LYP/TZVP vibrational frequencies. Computed $\nu(CO)$, $\nu(CN)_{asym}$, and $\nu(CN)_{sym}$ modes (Table 5) show several results. (i) All stretching frequencies are red-shifted upon bonding to sulfide, but whereas the differences in both CN modes are about 20 cm^{-1} per sulfur bond, the CO frequency decreases ∼120 cm^{-1} with one Et−S group and decreases ∼70 cm^{-1} further with a second Et−S group, a behavior found in all media. (ii) Increasing polarity produces also a red-shift, but whereas in both CN modes it is negligible, the CO stretching frequency decreases about 20 cm^{-1} in the isolated cofactor and 30 cm^{-1} in both sulfide-bound cofactors when going from vacuum to water. (iii) Comparison with isolated CN^- and CO diatomics reveals also a distinct qualitative behavior in both ligands for, whereas cyanide frequency is blue-shifted with a maximum difference of 84 cm^{-1} ($Fe(CN)_2CO$ in water), carbon monoxide is red-shifted yet with much greater differences (a maximum of 265 cm^{-1} for $(Et-S)_2-Fe(CN)_2CO$ in water). (iv) Since all the experimental frequencies correspond to the cofactor bound to two cysteines under biological conditions, our values for proper comparison should be those of $(Et-S)_2-Fe(CN)_2CO$ either in ε = 40 (outer protein regions) or in water (which are indeed virtually identical). Taking into account the usual performance of vibrational frequencies computed in DFT quantum calculations,[53] our B3LYP/TZVP results may be viewed as satisfactorily reliable, but the $\nu(CO)$ value that compares with experiment should be that in $Et-S-Fe(CN)_2CO$ rather than $(Et-S)_2-Fe(CN)_2CO$.

Taken together, these results indicate that CN ligands in the $Fe(CN)_2CO$ cofactor show a vibrational behavior not very different from isolated cyanide anions and insensitive to environmental effects. In contrast, CO ligand in the cofactor exhibits rather distinct features with a considerably lower vibrational stiffness upon bonding to iron and increasing the polarity of medium.

Table 5. B3LYP/TZVP Vibrational Frequencies of CO and CN Ligands in Species Involved in the Binding of $Fe(CN)_2CO$ Obtained in SCRF-PCM Calculations in Five Media of Different Polarity[a]

	ε = 1	ε = 2	ε = 4	ε = 40	ε: water
			$Fe(CN)_2CO$		
$\nu(CO)$	2091	2084	2079	2074	2074
$\nu(CN)_{asym}$	2148	2147	2147	2148	2148
$\nu(CN)_{sym}$	2149	2148	2148	2150	2150
			$Et-S-Fe(CN)_2CO$		
$\nu(CO)$	1975	1963	1955	1946	1945
$\nu(CN)_{asym}$	2128	2126	2125	2123	2122
$\nu(CN)_{sym}$	2130	2129	2128	2127	2127
			$(Et-S)_2-Fe(CN)_2CO$		
$\nu(CO)$	1906	1890	1881	1871	1870
$\nu(CN)_{asym}$	2102	2100	2098	2097	2096
$\nu(CN)_{sym}$	2107	2105	2104	2103	2103
			CO and CN^- Diatomics		
$\nu(CO)$	2142	2139	2137	2136	2135
$\nu(CN)$	2070	2066	2066	2066	2066
			IR experimental data[b]		
	A	B	C	D	E
$\nu(CO)$	1947	1957	1951	1969	1956
$\nu(CN)_{asym}$	2080	2076	2075	2077	2072
$\nu(CN)_{sym}$	2098	2088	2099	2099	2092

[a]All values in cm^{-1}. Computed frequencies corrected by the B3LYP/TZVP scaling factor 0.9654, ref 53. [b]Experimental values from different cofactors and proteins as follows. (A) NiFe final cofactor, wild-type hydrogenase from *R.eutropha*, ref 18; (B) NiFe final cofactor, hydrogenase from *Synechocystis* sp., ref 54; (C) $Fe(CN)_2CO$ cofactor, HypCD complex from *E. coli*, ref 15; (D) $Fe(CN)_2CO$ cofactor, HypCD complex from *R. eutropha*, ref 15; (E) $Fe(CN)_2CO$ cofactor, HypD isolated in the absence of HypC from *E. coli*, ref 13.

Cofactor Site in the HypCD Complex. Apart from the [4Fe−4S] cluster in HypD protein, the electron density used for determining the crystal structure of the HypCD complex from *T. kodakaraensis* did not allow additional cofactors to be modeled.[14] Isolation and crystallization of this complex in the presence of air might presumably result in loss of the oxygen-labile cofactors.[13] Besides, this crystal structure also lacks the first three amino acids of HypC, thus missing C2 which is well-known to be a crucial residue to bind the cofactor.[7,11,16] Upon reconstructing this HypCD complex as indicated in the Computational Methods section, the selection of residues within 3.0 Å of the cofactor yielded a close neighborhood consisting of C2 in HypC and C38, H41, H202, and F228 in HypD (Figure 3C). In agreement with the proposal by Watanabe and co-workers,[14] Fe is coordinated by HypC−C2 and HypD−C38 with distances $Fe-S_{C2}$ = 2.197 Å and $Fe-S_{C38}$ = 2.140 Å in this model. Two strongly conserved histidines H41 and H202 (C41, H44, and H201 in *E. coli* numbering) that have been proposed to play a role in binding the cofactor appear in the vicinity of C38 in HypD.[13,14] Although it is conventionally assumed that H202 should also bind an iron atom,[11,14,15] our model places these histidines not close enough for iron binding, although they are still within H-bond distances of cofactor ligands ($CN_1\cdots N_{\delta 1}-H202$ = 2.990 Å and $CN_2\cdots N_{\varepsilon 2}-H41$ = 2.590 Å). The lack of direct Fe−H202 binding should agree with the observation that a mutation of the conserved H202 did not affect the activity of [NiFe]-hydrogenase in *E. coli*.[55] The role of F228 is unclear, but its location approximately amidst H41 and H202 and its distance from H202 (∼4.0 Å) could suggest some type of stacking interaction with both imidazole rings. In any event, it is obvious that elucidating the detailed interactions in this site model deserves a further investigation which is beyond the scope of the current work.

dx.doi.org/10.1021/jp407574n | J. Phys. Chem. B 2013, 117, 13523−13533

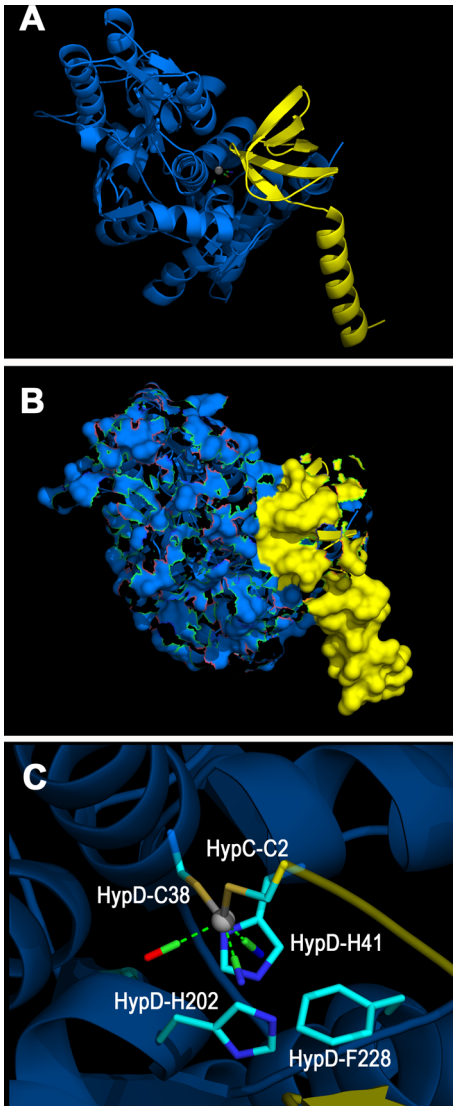

Figure 3. (A) Ribbon diagram of the crystal structure of the HypCD complex (HypC in yellow, HypD in blue) from *T. kodakaraensis* (PDB code 3VYR). (B) Molecular surface of the complex in the same geometry in part A. Surface holes correspond to missing residues in the electron density. (C) Model of the binding site of the $Fe(CN)_2CO$ cofactor (Fe, gray; C, green; N, blue; O, red) showing residues within 3.0 Å of the cofactor.

MD Simulation on HypC Protein from *R. leguminosarum*. The model structure of HypC from *R. leguminosarum* was generated by homology modeling from the HypC crystal structure from *T. kodakaraensis*.[11] Except for minor differences in the longer intersheet loop in the β-barrel domain, both structures are nearly identical. Particularly, side chains of the key C2 amino acid display a conformation virtually indistinguishable in both proteins (Figure S2 in the Supporting Information). The fact that HypC has been shown to act as a chaperone that guides the large subunit through the complete maturation process in *E. coli* has led to the proposal that this protein delivers the $Fe(CN)_2CO$ cofactor to the hydrogenase active site.[10−12,17,56] In the case of *R. leguminosarum*, HypC interacts with HupK, a scaffolding protein shown to act as an intermediate for incorporation of the cofactor in hydrogenases synthesized in the presence of oxygen.[22,57−59] This poses the question of the stability of the cofactor-bound form,[13] an issue which we have addressed with MD simulations for HypC from *R. leguminosarum* after including the cofactor structure obtained in the previous quantum calculations presented above. This way, the protein−ligand system is analyzed not only structurally but also dynamically.

The dynamical stability of the protein−cofactor−water−ions system along the 10 ns simulation is illustrated by temperature and total energy plots depicted in Figure S3 in the Supporting Information. Structural variations indicated by selected RMSD are shown in Figure 4. Besides the obvious C2 residue, we

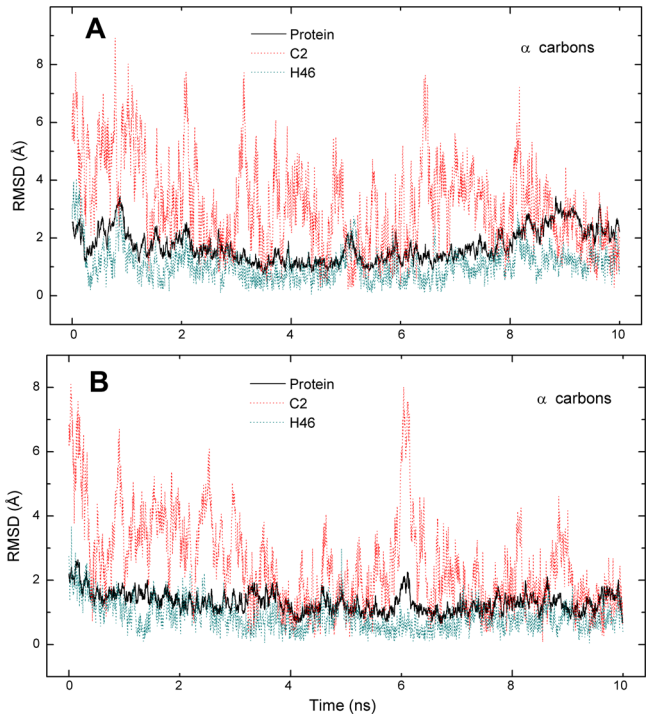

Figure 4. RMSD (α-carbons) of protein and residues C2 and H46 of the model structure of HypC from *R. leguminosarum* computed with respect to average structure along 10 ns MD simulations: (A) cofactor-free, isolated HypC; (B) cofactor-bound HypC protein.

included also H46 in the analysis because a function in the maturation process has been proposed for this strongly conserved histidine (H45 and H51 in *T. kodakaraensis* and *E. coli* numbering, respectively), although its role is still ambiguous.[11,13] Average RMSD values are the following (Å): protein = 1.724, C2 = 3.137, and H46 = 1.072 for the isolated cofactor-free form (Figure 4A) and protein = 1.316, C2 = 2.492, and H46 = 0.873 for the cofactor-bound form (Figure 4B). It is interesting to note that the cofactor−protein complex shows invariably lower RMSD values, particularly significant in the C2 residue. However, whereas the whole protein and H46 oscillate very little around their average values, C2 displays large oscillations during the greatest part of the simulation, especially in the isolated form. This should not be a surprising result if one considers that it is located at the end of an unstructured tail made of five residues that adopt an extended conformation (Figure 5). Note, however, that RMSD of C2 decreases significantly at ∼9 ns in both sets, showing values similar to those of H46 or the whole protein in the cofactor-bound form (Figure 4). These results suggest that the N-terminal tail of HypC stabilizes with time, an effect that is favored by the presence of the cofactor bound to C2. Since the whole protein

dx.doi.org/10.1021/jp407574n | J. Phys. Chem. B 2013, 117, 13523−13533

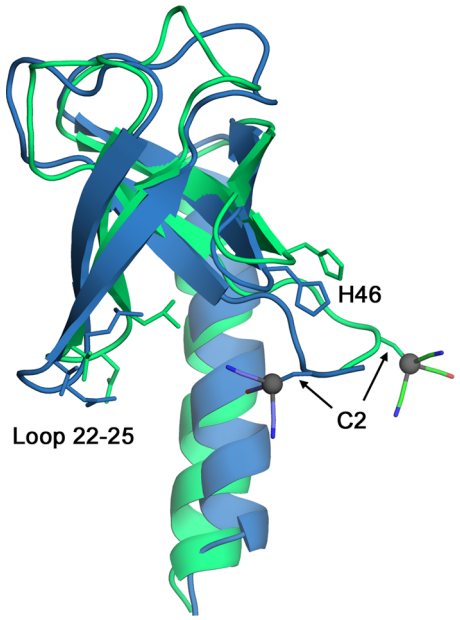

Figure 5. Superposition of initial (green) and final (blue) structures corresponding to the 10 ns MD simulation of the cofactor-bound form of model HypC protein from *R. leguminosarum*. C2, H46, and residues 22−25 in loop $\beta2-\beta3$ are drawn as sticks. In the $Fe(CN)_2CO$ cofactor: Fe, gray sphere; N, blue sticks; O, red sticks.

or the H46 residue which is located at the core of the protein (Figure 5) do not exhibit these trends, that stabilization should be viewed as a selective effect on the unstructured N-terminal tail.

B-factors calculated from root-mean-square fluctuations are plotted in Figure 6 together with the corresponding values of

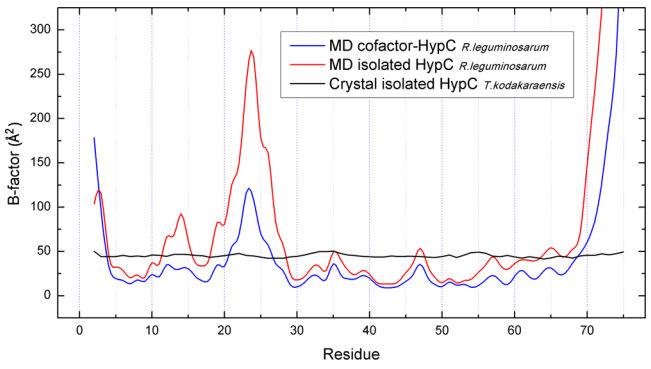

Figure 6. B-factors (backbone atoms) computed from 10 ns MD simulations for isolated and cofactor-bound forms of the model structure of HypC from *R. leguminosarum*. B-factors (α-carbons) in the crystal structure of isolated HypC from *T. kodakaraensis* (PDB code 2Z1C, ref 11) are plotted for reference.

the crystal structure of isolated HypC protein from *T. kodakaraensis*.[11] Average values are (Å^2) 78.25 and 35.70 for MD B-factors of isolated and cofactor-bound HypC, respectively, and 45.26 for the crystal structure, a magnitude indicative of certain local flexibility. When one considers motion in water, it is obvious that some parts of the structure such as loops or N- and C-terminal tails will show much greater fluctuations, as is indeed the case here. Apart from this, an interesting finding is that the cofactor-bound form of the *R. leguminosarum* HypC exhibits a clearly lower overall mobility than the isolated form with an average B-factor even smaller than the crystallographic value. The structural stability suggested by this result is significant in order to consider the role of HypC protein in either the delivery of the cofactor or its participation in the binding site in the HypCD complex. A striking result from the analysis of MD B-factors is the large fluctuations associated to residues 22−25 which make the loop joining $\beta2$ and $\beta3$ strands in the β-barrel domain of *R. leguminosarum* HypC (Figure 5). Although largely decreased in the cofactor-bound form, B-factors in these residues still reveal clearly greater mobility than the remaining residues.

The comparison between initial and final structures after the 10 ns MD simulation of the cofactor-bound model HypC from *R. leguminosarum* is shown in Figure 5. As it follows from the above discussion, the structure is kept unaltered except for the N-terminal tail and the orientation of bound $Fe(CN)_2CO$ which shows a significant displacement toward the structural protein core, a result which should be connected with the stabilization pointed out above. Although no obvious role is apparent for the H46 residue, it is interesting to note that the C2···H46 distance measured between the S atom in C2 and the nearest N atom in H46 in the initial structure (12.3 Å) decreases to half that value (5.85 Å) in the final structure. As for the loop defined by L22, D23, G24, and V25 residues which showed the greatest fluctuations in water, their side chains in initial and final structures are not so far distant. Only D23 among these residues is an amino acid expected to interact favorably with water and has in fact a side chain which protrudes into the aqueous environment. However, it is unclear whether this feature might account for the increased fluctuations of this loop.

CONCLUSIONS

The current model of the [NiFe] maturation process assumes a $Fe(CN)_2$ pre-cofactor linked to two cysteines in HypC and HypD proteins in the HypCD complex and a subsequent addition of CO. Quantum calculations used to investigate the changes occurring in all the species involved in the assembly of $Fe(CN)_2CO$ in the binding site of the HypCD complex showed that the addition of CO does not distort significantly the structure of $Fe(CN)_2$ when only one cysteine binds the Fe atom, whereas it changes from a tetrahedral arrangement to a square pyramidal structure when two cysteines bind the cofactor. The topological analysis of the electron density revealed that all links with the Fe atom are non-bonded interactions with features indicative of covalent contributions. Binding to sulfide produced differences between Fe−CN and Fe−CO bonds in the sense of introducing a π-character in iron−cyanide links. These results point thus to an ionic attraction with participation of covalent bonding between iron and cysteines in the binding site of the HypCD complex.

Effects arising from different polarities of the medium on the vibrational stretching frequencies of CO and CN ligands used as evidence of the presence of $Fe(CN)_2CO$ cofactor studied by means of SCRF-PCM calculations showed a markedly distinct behavior of carbon monoxide with regard to cyanide ligands. Large decreases in CO stretching frequencies were observed upon bonding to sulfide and increasing polarity of the medium. These changes were particularly noticeable when compared with the isolated diatomic reference frequency. Carbon monoxide thus exhibited a lower vibrational stiffness in the cofactor bound to cysteines in polar environments such as those expected in the binding site of the HypCD complex or

dx.doi.org/10.1021/jp407574n | J. Phys. Chem. B 2013, 117, 13523−13533

along its delivery mediated by the HypC protein in an aqueous environment. In contrast, these red-shifts were found to be scarcely significant in the CN stretching modes.

Using our cofactor-bound model structure of HypC protein from *R. leguminosarum*, a model of the active site of the crystal structure available for the HypCD complex from *T. kodakaraensis* was proposed. In this model, the iron atom of $Fe(CN)_2CO$ is coordinated by HypC−C2 and HypD−C38 within a 3 Å neighborhood defined by H41, H202, and F228 amino acids of HypD. However, without direct binding with iron, our model placed both histidines within H-bond distances from cofactor ligands.

Finally, since HypC plays a role in binding the cofactor and it is assumed to be part of a multiprotein complex mediating protein recognition, MD simulations were used to investigate the stability of cofactor-free and cofactor-bound forms of the HypC protein from *R. leguminosarum*. In both forms, HypC showed a marked structural stability in water, increased when the cofactor is bound, with small RMSD values for the whole protein of 1.724 and 1.316 Å for isolated and cofactor-bound forms, respectively. The N-terminal C2 residue which is known to bind the cofactor exhibited large motion along most of the MS simulation, a result arising from the fact that it is placed at the end of a tail made of residues in extended conformations. However, this N-terminal tail stabilizes with time, particularly in the presence of the $Fe(CN)_2CO$ cofactor bound to C2. In summary, our MD study demonstrated that, although the large motion of C2 might suggest the need for a guiding interaction in order to achieve the delivery of the cofactor to a receptor protein, the HypC−cofactor complex is stable enough to support the role of HypC protein in either that delivery or its participation in the binding site in the HypCD complex.

■ ASSOCIATED CONTENT

Supporting Information

CHARMM residue topology and parameter files for $Fe(CN)_2CO$ cofactor; CHelpG atomic charges for all species involved in formation and binding of the cofactor; figure with atom numbering in $(Et-S)_2-Fe(CN)_2CO$; figure showing the superposition of the model structure of *R. leguminosarum* and the crystal structure of *T. kodakaraensis* HypC proteins; plots of temperature and total energy along the 10 ns MD simulation of the cofactor-bound form of *R. leguminosarum* HypC; complete refs 29 and 30. This material is available free of charge via the Internet at http://pubs.acs.org.

■ AUTHOR INFORMATION

Corresponding Author

*E-mail: luis.fpacios@upm.es. Phone: 34-91-3364542.

Notes

The authors declare no competing financial interest.

■ ACKNOWLEDGMENTS

We deeply thank Prof. Jorge Seminario and Dr. Dahiyana Cristancho (Texas A&M University) for their help in kindly providing us the force constants set for $Fe(CN)_2CO$ cofactor obtained with an unreleased new version of their program FUERZA. We also thank Madrid Supercomputing and Visualization Center (CeSViMa) for providing supercomputer resources (Magerit cluster), technical expertise, and assistance under projects G52225 and G52234. The authors acknowledge financial support as follows: M.A. from Microambiente-CM project, J.-M.P. from the Spanish Ministry of Science, project BIO2010-15301, J.I. from Fundación Ramón Areces, XV Concurso Nacional de Ayuda para la Investigación en Ciencias de la Vida y de la Materia, and L.F.P. from the Spanish Ministry of Science, project BIO2009-07050.

■ REFERENCES

(1) Vignais, P. M.; Billoud, B. Occurence, Classification, and Biological Function of Hydrogenases: An Overview. *Chem. Rev.* **2007**, *107*, 4206−4272.

(2) Volbeda, A.; Charon, M. H.; Piras, C.; Hatchikian, E. C.; Frey, M.; Fontecilla-Camps, J. C. Crystal Structure of the Nickel-iron Hydrogenase from *Desulfovibrio gigas*. *Nature* **1995**, *373*, 580−587.

(3) Fontecilla-Camps, J. C.; Volbeda, A.; Cavazza, C.; Nicolet, Y. Structure-function Relationships of [NiFe] and [FeFe] Hydrogenases. *Chem. Rev.* **2007**, *107*, 4273−4303.

(4) Ogata, H.; Kellers, P.; Lubitz, W. The Crystal Structure of the [NiFe] Hydrogenase from the Photosynthetic Bacterium *Allochromatium vinosum*: Characterization of the Oxidized Enzyme (Ni-A State). *J. Mol. Biol.* **2010**, *402*, 428−444.

(5) Fritsch, J.; Scheerer, P.; Frielingsdorf, S.; Kroschinsky, S.; Friedrich, B.; Lenz, O.; Spahn, C. M. T. The Crystal Structure of an Oxygen-tolerant Hydrogenase Uncovers a Novel Iron-sulphur Centre. *Nature* **2011**, *479*, 249−253.

(6) Volbeda, A.; Amara, P.; Darnault, C.; Mouesca, J. M.; Parkin, A.; Roessler, M. M.; Armstrong, F. A.; Fontecilla-Camps, J. C. X-ray Crystallographic and Computational Studies of the O_2-tolerant [NiFe] Hydrogenase 1 from *Escherichia coli*. *Proc. Natl. Acad. Sci. U.S.A.* **2012**, *109*, 5305−5310.

(7) Böck, A.; King, P. W.; Blokesch, M.; Posewitz, M. C. Maturation of Hydrogenases. *Adv. Microbiol. Physiol.* **2006**, *51*, 1−71.

(8) Olson, J. W.; Mehta, N. S.; Maier, R. J. Requirement of Nickel Metabolism Proteins HypA and HypB for Full Activity of Both Hydrogenase and Urease in *Helicobacter pylori*. *Mol. Microbiol.* **2001**, *39*, 176−182.

(9) Blokesch, M.; Albracht, S. P. J.; Matzanke, B. F.; Drapal, N. M.; Jacobi, A.; Böck, A. The Complex Between Hydrogenase Maturation Proteins HypC and HypD is an Intermediate in the Supply of Cyanide to the Active Site Iron of [NiFe] Hydrogenases. *J. Mol. Biol.* **2004**, *344*, 155−167.

(10) Lenz, O.; Ludwig, M.; Schubert, T.; Bürstel, I.; Ganskow, S.; Goris, T.; Schwarze, A.; Friedrich, B. H_2 Conversion in the Presence of O_2 as Performed by the Membrane-bound [NiFe] Hydrogenase of *Ralstonia eutropha*. *ChemPhysChem* **2010**, *11*, 1107−111.

(11) Watanabe, S.; Matsumi, R.; Arai, T.; Atomi, H.; Imanaka, T.; Miki, K. Crystal Structures of [NiFe] Hydrogenase Maturation Proteins HypC, HypD, and HypE: Insights into Cyanation Reaction by Thiol Redox Signaling. *Mol. Cell* **2007**, *27*, 29−40.

(12) Soboh, B.; Stripp, S. T.; Muhr, E.; Granich, C.; Braussemann, M.; Herzberg, M.; Heberle, J.; Sawers, R. G. [NiFe]-Hydrogenase Maturation: Isolation of a HypC-HypD Complex Carrying Diatomic CO and CN^- Ligands. *FEBS Lett.* **2012**, *586*, 3882−3887.

(13) Stripp, S. T.; Soboh, B.; Lindenstrauss, U.; Braussemann, M.; Herzberg, M.; Nies, D. H.; Sawers, R. G.; Heberle, J. HypD is the Scaffold Protein for $Fe(CN)_2CO$ Cofactor Assembly in [NiFe] Hydrogenase Maturation. *Biochemistry* **2013**, *52*, 3289−3296.

(14) Watanabe, S.; Matsumi, R.; Atomi, H.; Imanaka, T.; Miki, K. Crystal Structures of the HypCD Complex and the HypCDE Ternary Complex: Transient Intermediate Complexes During [NiFe] Hydrogenase Maturation. *Structure* **2012**, *20*, 2124−2137.

(15) Bürstel, I.; Siebert, E.; Winter, G.; Hummel, P.; Zebger, I.; Friedrich, B.; Lenz, O. A Universal Scaffold for Synthesis of the $Fe(CN)_2CO$ Moiety of [NiFe] Hydrogenase. *J. Biol. Chem.* **2012**, *287*, 38845−38853.

(16) Blokesch, M.; Böck, A. Maturation of [NiFe]-Hydrogenases in *Escherichia coli*: the HypC Cycle. *J. Mol. Biol.* **2002**, *324*, 287−296.

(17) Forzi, L.; Sawers, R. G. Maturation of [NiFe]-Hydrogenases in *Escherichia coli*. *BioMetals* **2007**, *20*, 565−578.

(18) Rippers, Y.; Utesch, T.; Hildebrant, P.; Zebger, I.; Mroginski, M. A. Insights Into the Structure of the Active Site of the O_2-tolerant Membrane Bound [NiFe] Hydrogenase of *R. eutropha* H16 by Molecular Modelling. *Phys. Chem. Chem. Phys.* **2011**, *13*, 16146−16149.
(19) Tomasi, J.; Mennucci, B.; Cammi, R. Quantum Mechanical Continuum Solvation Models. *Chem. Rev.* **2005**, *105*, 2999−3093.
(20) Manyani, H.; Rey, L.; Palacios, J. M.; Imperial, J.; Ruiz-Argüeso, T. Gene Products of the *hupGHIJ* Operon are Involved in Maturation of the Iron-sulfur Subunit of the [NiFe] Hydrogenase from *Rhizobium leguminosarum* bv. viciae. *J. Bacteriol.* **2005**, *187*, 7018−6026.
(21) Brito, B.; Prieto, R. I.; Cabrera, E.; Mandrand-Berthelot, M. A.; Imperial, J.; Ruiz-Argüeso, T.; Palacios, J. M. *Rhizobium leguminosarum hupE* Encodes a Nickel Transporter Required for Hydrogenase Activity. *J. Bacteriol.* **2010**, *192*, 925−935.
(22) Albareda, M.; Manyani, H.; Imperial, J.; Brito, B.; Ruiz-Argüeso, T.; Böck, A.; Palacios, J. M. Dual Role of HupF in the Biosynthesis of [NiFe] Hydrogenase in *Rhizobium leguminosarum*. *BMC Microbiol.* **2012**, *12*, 256−268.
(23) Weigend, F.; Ahlrichs, R. Balanced Basis Sets of Split Valence, Triple Zeta Valence and Quadruple Zeta Valence Quality for H to Rn: Design and Assessment of Accuracy. *Phys. Chem. Chem. Phys.* **2005**, *7*, 3297−3305.
(24) Li, L.; Li, C.; Zhang, Z.; Alexov, E. On the Dielectric "Constant" of Proteins: Smooth Dielectric Function for Macromolecular Modeling and its Implementation in DelPhi. *J. Chem. Theory Comput.* **2013**, *9*, 2126−2136.
(25) Breneman, C. M.; Wiberg, K. B. Determining Atom-centered Monopoles from Molecular Electrostatic Potentials. The Need for High Sampling Density in Formamide Conformational Analysis. *J. Comput. Chem.* **1990**, *11*, 361−373.
(26) Bader, R. F. W. *Atoms in Molecules: A Quantum Theory*; Clarendon: Oxford, U.K., 1990.
(27) Popelier, P. *Atoms in Molecules: An Introduction*; Prentice-Hall: Harlow, U.K., 2000.
(28) Biegler-Konig, F. W.; Bader, R. F. W.; Hang, T. H. Calculation of the Average Properties of Atoms in Molecules. II. *J. Comput. Chem.* **1982**, *3*, 317−328.
(29) Frisch, M. J.; Trucks, G. W.; Schlegel, H. B.; Scuseria, G. E.; Robb, M. A.; Cheeseman, J. R.; Scalmani, G.; Barone, V.; Mennucci, B.; Petersson, G. A.; et al. *Gaussian 09*, revision A.02; Gaussian, Inc.: Wallingford, CT, 2009.
(30) MacKerell, A. D.; Bashford, D.; Bellott, M.; Dunbrack, R. L.; Evanseck, J.; Field, M. J.; Fischer, S.; Gao, J.; Guo, H.; Ha, S.; et al. All-atom Empirical Potential for Molecular Modeling and Dynamics Studies of Proteins. *J. Phys. Chem. B* **1998**, *102*, 3586−3616.
(31) Zoete, V.; Cuendet, M. A.; Grosdidier, A.; Michielin, O. SwissParam, a Fast Force Field Generation Tool for Small Organic Molecules. *J. Comput. Chem.* **2011**, *32*, 2359−2368.
(32) Seminario, J. M. Calculation of Intramolecular Force Fields from Second-derivative Tensors. *Int. J. Quantum Chem.* **1996**, *30*, 1271−1277.
(33) Bautista, E. J.; Seminario, J. M. Harmonic Force Field for Glycine Oligopeptides. *Int. J. Quantum Chem.* **2008**, *108*, 180−188.
(34) Smith, D. M. A.; Xiong, Y.; Straatsma, T. P.; Rosso, K. M.; Squier, T. C. Force-field Development and Molecular Dynamics of [NiFe] Hydrogenase. *J. Chem. Theory Comput.* **2012**, *8*, 2103−2114.
(35) Arnold, K.; Bordoli, L.; Kopp, J.; Schwede, T. The SWISS-MODEL Workspace: A Web-based Environment for Protein Structure Homology Modelling. *Bioinformatics* **2006**, *22*, 195−201.
(36) Kiefer, F.; Arnold, K.; Künzli, M.; Bordoli, L.; Schwede, T. The SWISS-MODEL Repository and Associated Resources. *Nucleic Acids Res.* **2009**, *37*, D387−D392.
(37) Benkert, P.; Biasini, M.; Schwede, T. Toward the Estimation of the Absolute Quality of Individual Protein Structure Models. *Bioinformatics* **2011**, *27*, 343−350.
(38) Guex, N.; Peitsch, M. C. SWISS-MODEL and the Swiss-PdbViewer: An Environment for Comparative Protein Modeling. *Electrophoresis* **1997**, *18*, 2714−2723.
(39) Pettersen, E. F.; Goddard, T. D.; Huang, C. C.; Couch, G. S.; Greenblatt, D. M.; Meng, E. C.; Ferrin, T. E. UCSF Chimera - a Visualization System for Exploratory Research and Analysis. *J. Comput. Chem.* **2004**, *25*, 1605−1612.
(40) Humphrey, W.; Dalke, A.; Schulten, K. VMD: Visual Molecular Dynamics. *J. Mol. Graphics* **1996**, *14*, 33−38.
(41) Phillips, J. C.; Braun, R.; Wang, W.; Gumbart, J.; Tajkhorshid, E.; Villa, E.; Chipot, C.; Skeel, R. D.; Kalé, L.; Schulten, K. Scalable Molecular Dynamics with NAMD. *J. Comput. Chem.* **2005**, *26*, 1781−1802.
(42) Kozakov, D.; Hall, D. R.; Beglov, D.; Brenke, R.; Comeau, S. R.; Shen, Y.; Zheng, J.; Vakili, P.; Paschalidis, I. C.; Vajda, S. Achieving Reliability and High Accuracy in Automated Protein Docking: Cluspro, PIPER, SDU, and Stability Analysis in CAPRI Rounds. *Proteins: Struct., Funct., Bioinf.* **2010**, *78*, 3124−3130.
(43) Jorgensen, W. L.; Chandrasekhar, J.; Madura, J. D.; Impey, R. W.; Klein, M. L. Comparison of Simple Potential Functions for Simulating Liquid Water. *J. Chem. Phys.* **1983**, *79*, 926−935.
(44) Darden, T.; York, D.; Pedersen, L. Particle Mesh Ewald: An *N*-log(*N*) Method for Ewald Sums in Large Systems. *J. Chem. Phys.* **1993**, *98*, 10089−10092.
(45) Glykos, N. M. Carma: A Molecular Dynamics Analysis Program. *J. Comput. Chem.* **2006**, *27*, 1765−1768.
(46) Popov, A. V.; Vorobjev, Y. N.; Zharkov, D. O. MDTRA: A Molecular Dynamics Trajectory Analyzer with a Graphical User Interface. *J. Comput. Chem.* **2013**, *34*, 319−325.
(47) *PyMOL*, version 1.5.0.4; The PyMOL molecular graphics system; Schrödinger LLC: New York, 2013.
(48) Shomura, Y.; Yoon, K. S.; Nishihara, H.; Higuchi, Y. Structural Basis for a [4Fe-3S] Cluster in the Oxygen-tolerant Membrane-bound [NiFe] Hydrogenase. *Nature* **2011**, *479*, 253−256.
(49) Pacios, L. F. Changes of Electron Properties in the Formation of Hydrogen Bonds. In *Hydrogen bonding - New insights*; Grabowski, S. J., Ed.; Series: Challenges and Advances in Computational Chemistry and Physics, Vol. *3*; Springer: New York, 2006; Chapter 3, pp 109−148.
(50) Arnold, W. D.; Oldfield, E. The Chemical Nature of Hydrogen Bonding in Proteins Via NMR: J-couplings, Chemical Shifts, and AIM Theory. *J. Am. Chem. Soc.* **2000**, *122*, 12835−12841.
(51) Pacios, L. F.; Gómez, P. C. Dependence of Calculated NMR Proton Chemical Shifts on Electron Density Properties in Proton-transfer Processes on Short Strong Hydrogen Bonds. *J. Phys. Chem. A* **2004**, *108*, 11783−11792.
(52) Pacios, L. F.; Gálvez, O.; Gómez, P. C. Variation of Geometries and Electron Properties Along Proton Transfer in Strong Hydrogen-bond Complexes. *J. Chem. Phys.* **2005**, *122*, 214307−214311.
(53) Scott, A. P.; Radom, L. Harmonic Vibrational Frequencies: An Evaluation of Hartree-Fock, Moller-Plesset, Quadratic Configuration Interaction, Density Functional Theory and Sempiempirical Scale Factors. *J. Phys. Chem.* **1996**, *100*, 16502−16526.
(54) Germer, F.; Zebger, I.; Saggu, M.; Lendzian, F.; Schulz, R.; Appel, J. Overexpression, Isolation, and Spectroscopic Characterization of the Bidirectional [NiFe] Hydrogenase from *Synechocystis* sp. PCC 6803. *J. Biol. Chem.* **2009**, *284*, 36462−36472.
(55) Blokesch, M.; Böck, A. Properties of the [NiFe] Hydrogenase Maturation Protein HypD. *FEBS Lett.* **2006**, *580*, 4065−4068.
(56) Drapal, N.; Böck, A. Interaction of the Hydrogenase Accessory Protein HypC with HypE, the Large Subunit of *Escherichia coli* Hydrogenase 3 During Enzyme Maturation. *Biochemistry* **1998**, *37*, 2941−2948.
(57) Imperial, J.; Rey, L.; Palacios, J. M.; Ruiz-Argüeso, T. HupK, a Hydrogenase-Ancillary Protein from *Rhizobium leguminosarum*, Shares Structural Motifs with the Large Subunit of NiFe Hydrogenases and Could Be a Scaffolding Protein for Hydrogenase Metal Cofactor Assembly. *Mol. Microbiol.* **1993**, *9*, 1305−1306.
(58) Ludwig, M.; Schubert, T.; Zebger, I.; Wisitruangsakul, N.; Saggu, M.; Strack, A.; Lenz, O.; Hildebrant, P.; Friedrich, B. Concerted Action of Two Novel Auxiliary Proteins in Assembly of the Active Site in a Membrane-bound [NiFe] Hydrogenase. *J. Biol. Chem.* **2009**, *284*, 2159−2168.

(59) Albareda, M.; Manyani, H.; Pacios, L. F.; Rey, L.; Brito, B.; Ruiz-Argüeso, T.; Imperial, J.; Palacios, J. M. Functional Roles of HypC and HupK in the Biosynthesis of [NiFe] Hydrogenase in *Rhizobium leguminosarum*. In The 10th International Hydrogenase Conference; Szeged, Hungary, 2013; Session 3, Paper 5.